Estimation of laser-induced damage depth from surface image features

Guillaume Hallo, Yanis Abdelmoumni-Prunes, Sylvain Grosjean, Jérôme Néauport, Chloé Lacombe, Laurent Lamaignère, François Hild

Estimation of laser-induced damage depth from surface image features

GUILLAUME HALLO,[1,2] YANIS ABDELMOUMNI-PRUNES,[1] SYLVAIN GROSJEAN,[1] JÉRÔME NÉAUPORT,[1] CHLOÉ LACOMBE,[1,*] LAURENT LAMAIGNÈRE,[1] AND FRANÇOIS HILD[2]

[1]*CEA, CESTA, F-33116, Le Barp, France*
[2]*Université Paris-Saclay, CentraleSupélec, ENS Paris-Saclay, CNRS, LMPS - Laboratoire de Mécanique Paris-Saclay, 91190 Gif-sur-Yvette, France*
[*]*chloe.lacombe@cea.fr*

Abstract: In laser damage experiments, damage initiation and growth are typically monitored by imaging the surface of the tested fused silica sample, ignoring their bulk morphology. The depth of a damage site in fused silica optics is considered to be proportional to its equivalent diameter. However, some damage sites experience phases with no diameter changes but growth in the bulk independently from their surface. A proportionality relationship with the damage diameter does not accurately describe the growth of such sites. In the following, an accurate estimator for damage depth is proposed, which is based on the hypothesis that the light intensity scattered by a damage site is proportional to its volume. Such an estimator, using the pixel intensity, describes the change of damage depth through successive laser irradiations, including phases where depth and diameter variations are uncorrelated.

1. Introduction

Fused silica optics are prone to damage when exposed to high-fluence laser beams at UV wavelength and ns pulse duration [1]. Once a damage site has initiated, it grows after each laser shot with an energy greater than a growth threshold [2]. Damage initiation and growth are phenomena that limit the operation of high-power laser installations such as those designed to achieve fusion by inertial confinement [3, 4]. Damage experiments were thus conducted to show that the damage growth probability was dependent on laser fluence, pulse duration, laser wavelength and damage size among other properties [5–8]. To quantify damage growth, images of damage sites are acquired through the face of the tested sample and sizes are estimated through pixel-counting on binarized images [6, 9]. Damage sites take the form of highly fractured craters [10, 11]. The knowledge of the morphology of the crater in terms of lateral dimension and depth is useful for the development of mitigation techniques [12, 13] or when the optical component is a vacuum window that may break [14, 15]. The depth of a damage site is considered to be a proportion of its equivalent diameter on the face of the sample, namely, a 3^{rd} for fracture depth, a 5^{th} for the crater depth [10]. However, experimental results have underlined the existence of phases with constant apparent damage size on sample surfaces while damage grew in depth (*i.e.,* so-called Veinhard plateaus [16]). The relationship between damage depth and equivalent diameter is thus not always linear, thereby underlying that fused silica crack growth is a stochastic phenomenon [17].

Imaging the volume of a damage site to get a better knowledge of its growth is not straight forward as it needs dedicated sample preparation [10, 16], or complex equipment such as confocal microscopes [18, 19]. Further, measuring the depth of damage sites in brittle materials such as fused silica by top view defocused images is inaccurate due to multiple reflections induced by complex damage patterns. Therefore, an accurate damage depth estimator using only surface images is desirable to quantify damage growth. The analysis of gray levels in non-binarized

surface images has proven to be more accurate than pixel-counting as a means of determining equivalent damage diameters [20]. It was also shown that, during Veinhard plateaus, the gray levels in surface images increased [21]. Besides, gray-level analyses have also been shown to enable for the detection of damage growth earlier than pixel-counting methods on binarized images [22].

In the following, it is proposed to provide gray level analyses in conjunction with pixel-counting to obtain a robust damage depth estimator only based on non-binarized images of surfaces. A laser damage growth experiment was conducted on four different damage sites on a highly instrumented optical setup (Section 2.1). A traditional surface imaging, as well as from the side of the sample, make it possible to measure both damage diameter and depth between each laser shot. Two of these four sites experienced the aforementioned Veinhard plateau phases. A series of corrections was applied to ensure that all the images in a sequence were comparable (Section 2.2). Relevant features were extracted from images, namely, surface diameters and sum of pixel intensities (Section 2.3). An estimator for damage depth was then inferred from these two surface features. Such estimator is based on the hypothesis that the light intensity scattered by a damage site is proportional to its volume. The proposed depth estimator was tested for four different damage sites (Section 3).

2. Materials and methods

Damage growth sequences were conducted on the laser damage setup MELBA [23]. Both surface and bulk images were acquired during growth experiments with tunable laser parameters. A dedicated sample with polished edges without beveled corners was needed to acquire bulk images. The acquired images were processed to correct for camera motions between acquisitions, gray level variations and focus changes. Damage features were extracted from corrected images such as damage diameter, sum of pixel intensities from images of the surface and damage depth from bulk images. Such features were analyzed in order to estimate damage depth only from surface data.

2.1. Laser damage set-up

MELBA is a laser damage test setup designed for the metrology of laser damage initiation and growth. It delivers a 351 nm laser beam with up to 9 mm in diameter and customizable temporal and spatial profiles [24]. For previous laser damage experiments, a fused silica sample was polished on one of its lateral sides [16, 25]. As a complement to standard surface imaging, a camera was added on the side of the sample to provide pseudo-volume images describing damage sites in the sample bulk (Figure 1).

The imaging system used to acquire images of the surface was a Leica M420 macroscope, set up to have a pixel size of 6.45 µm in the object plane. Volume imaging was based on a Navitar Zoom 6000 lens system coupled with a CCD camera, with a pixel size of 2.28 µm in the object plane. The sample was lit by a white LED bar on one of its edges during damage growth sequences. The lighting system was the same for both imaging systems.

Four damage sites were initiated on the silica sample by setting a phase ring in the laser beam to provide a high fluence spot on the sample. For image correction purposes, three surface fiducials were initiated on the surface of the sample near each damage site using the laser beam of the MELBA setup. Such surface fiducials were visible on surface images but not in volume images. Bulk fiducials, were initiated in the bulk of the sample using a laser beam with a pulse duration of 0.8 ps at a wavelength of 1054 nm [26]. The bulk engraving method was similar to the process described in Ref. [27]. The laser beam was focused at several depths varying between 0 and 1 mm below the surface of the sample (Figure 5 in Appendix).

The four damage sites were then subjected to a growth sequence consisting of 250 to 450 laser shots at an incidence of a few degrees with mean fluence ranging between 1 and 8 J/cm^2. Both

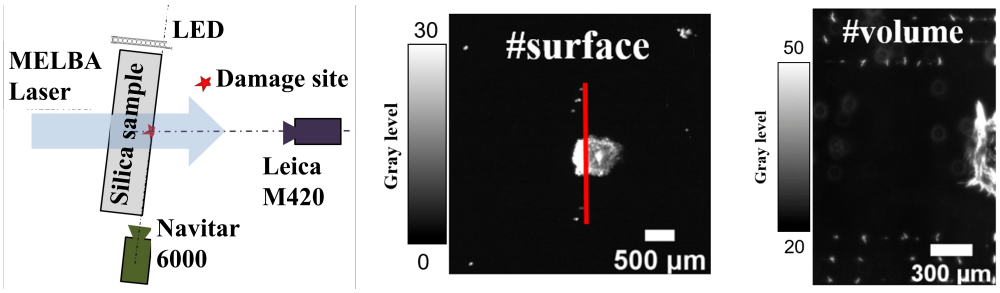

(a) (b) (c)

Fig. 1. (a) Imaging system used on the MELBA experimental setup to perform damage growth sequences and acquire images of surface and bulk of damage sites. The surface camera was moved in front of the sample after each laser shot and removed before the next one. Images of the surface with Leica M420 macroscope (b) and bulk with Navitar 6000 and CCD camera (c) of a damage site were acquired after each laser shot. The image plane of the bulk image is represented by the red line in the surface image. Example of images taken on site 1 after shot # 218/413

surface and volume images were captured between eachlaser shot. The MELBA beam diameter was approximately 6 mm on the sample surface. To avoid growth on surface and bulk fiducials, the spatial shape of the beam was locally shadowed in order not to irradiate them during the growth sequence. The damage sites were subjected to temporally square laser pulses, with a pulse duration of 5 ns flat in time for sites 1 and 2, and 10 ns flat in time for sites 3 and 4 (thereby ensuring a variety of lighting conditions). The fluence was regularly modified between every laser shot in order to ensure slow and gradual damage growth.

2.2. Image corrections

Throughout the growth sequence, images were affected by disturbances such as displacements, spurious light and focus changes. In order to ensure that the images are comparable during the whole sequence, with differences between them only caused by damage growth, all of those changes had to be corrected [28]. Displacements between images were corrected using Digital Image Correlation [29]. Brightness and contrast corrections were applied to reduce the effect of lighting variations [30]. Then, the images were convolved by a Gaussian kernel whose standard deviation was adjusted to equalize sharpness levels throughout the image sequence. Such corrections, fully described in the Appendix, were needed to exploit gray levels and to ensure that the damage segmentation process was consistent throughout the sequence.

2.3. Feature extraction

To extract relevant features from both surface and volume images, the first step was to determine the outline of the main damage site in every image. In both types of images, the segmentation method was the same. An example of the proposed segmentation process of a volume image is shown in Figure 2.

First, the outline of the damage site and its fractures were intensified through the use of a Sato filter [31] (Figure 2(b)). Originating from medical image analysis, the Sato filter was designed to identify curvilinear structures, and it is thus adapted to heavily-fractured laser damage sites. The output of the filter was then subjected to a global thresholding, which, after contour selection, resulted in a mask containing the main damage site (Figure 2(c)). The specific parameters of the Sato filter and thresholding were determined empirically, and were the same for every damage

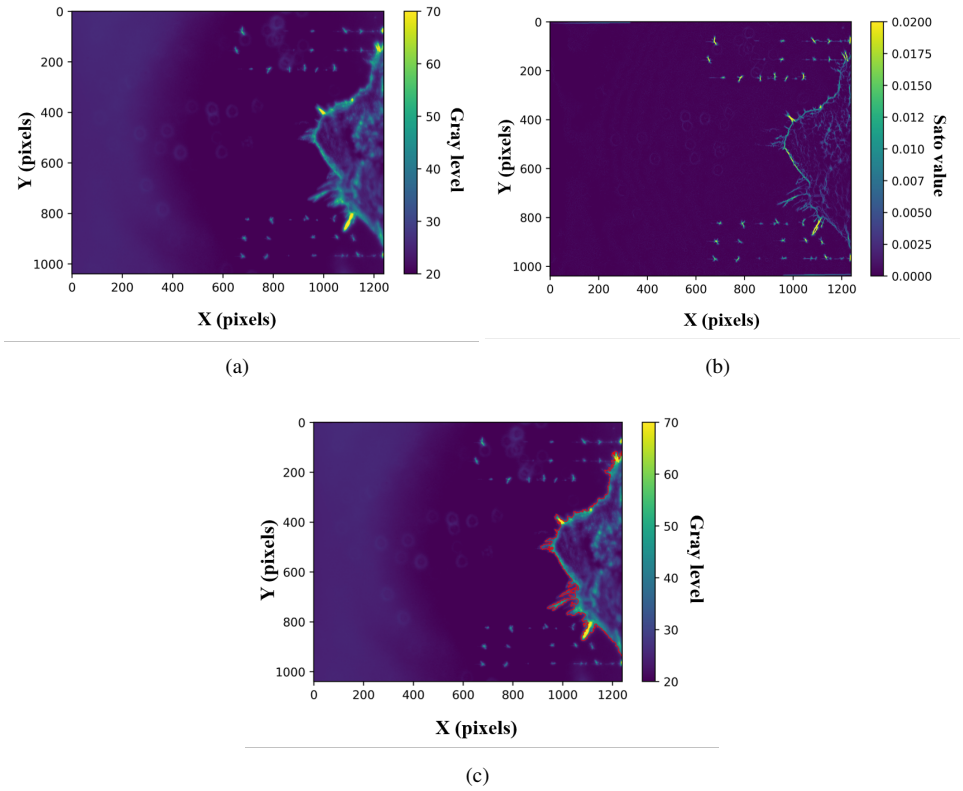

Fig. 2. Steps of the segmentation process for a volume image: (a) original image of site 2 acquired after shot # 394/412, (b) output of Sato filter and (c) resulting contour in red. Filtering allows laser damage features to be isolated from the background and bulk fiducials

site (although they differed between surface and volume images, as their dynamic ranges were different).

The obtained mask was used for pixel-counting in surface images, which yielded the apparent damage area A, as well as its equivalent diameter d

$$d = 2\sqrt{\frac{A}{\pi}}. \tag{1}$$

For each surface image, the RMS residual and the sum of pixel intensities were extracted from the damage mask. In volume images, the depth of the damage site was estimated with the farthest point to the surface of the sample in the damage mask. The values for damage depth, surface and equivalent diameter were converted into micrometers to be expressed on the same scale.

In order to estimate the depth of a damage site from surface features (*i.e.,* damage diameter and sum of pixel intensities), it was assumed that the light intensity scattered by a damage site was proportional to its volume

$$TIS = \alpha V_d, \tag{2}$$

where TIS (Total Integrated Signal) is the sum of pixel intensities (*i.e.,* a part of the scattered light by the damage site), V_d the volume of the damage site, and α a proportionality coefficient. Assuming that the shape of the crater of a damage site was similar to that of a spherical dome,

the volume of a damage site is written as

$$V_d \approx \frac{\pi}{6}\left(\frac{3}{4}d^2\delta + \delta^3\right), \tag{3}$$

where δ is the maximum depth of the damage site.

From Equations (2) and (3), a cubic equation is obtained

$$\delta^3 + \frac{3}{4}d^2\delta - \frac{6}{\alpha\pi}TIS = 0 \tag{4}$$

The unique real damage depth solution, δ_s, to Equation (4) reads

$$\delta_s = \sqrt[3]{\frac{3TIS}{\alpha\pi} + \sqrt{\frac{3d^4}{1024} - 8\frac{TIS^3}{(\alpha\pi)^3}}} + \sqrt[3]{\frac{3TIS}{\alpha\pi} - \sqrt{\frac{3d^4}{1024} - 8\frac{TIS^3}{(\alpha\pi)^3}}} \tag{5}$$

The proportionality factor α was estimated using a linear fit for damage site 1, and was equal to $6 \times 10^{-3}\,\mathrm{GL}/\mu\mathrm{m}^3$.

3. Results and discussion

The estimators of damage depth based on the fraction of damage diameter or on the proposed model (Equation (5)) were evaluated according to the R^2 scores reported in Table 1. The R^2 score, or Pearson correlation coefficient, quantifies the quality of a linear regression [32]. A perfect regression involves an R^2 score equal to 1. The best fraction of damage diameter was evaluated to be $\frac{1}{2.32}$ for these four damage sites. Such fraction is close to $\frac{1}{3}$ reported in Ref. [10]. Thus, the damage sites studied in this paper were representative of those evaluated in the afore-cited reference.

Table 1. R^2 score on each site for both depth estimators (best fraction of diameter and Equation (5)).

	R^2 score			
Depth estimator	Site 1	Site 2	Site 3	Site 4
Equation (5)	0.96	0.95	0.96	0.96
Best fraction of diameter	0.81	0.98	0.98	0.99

The R^2 scores were calculated between the true depth measured on the images (in green in Figures 3 and 4) and that given by the different estimators, namely, best fraction of diameter, $\frac{1}{2.32}$ (in red) or the proposed equation (in blue). Sites 2, 3 and 4 were well described by the depth estimator based on a fraction of diameter, with R^2 scores ranging between 0.98 and 0.99. The depth of site 1 on the other hand could not be described solely with a constant fraction of damage diameter, as shown by an R^2 score of only 0.81, mainly because of a large Veinhard plateau during the growth sequence. Such phase is observed in **Visualization 1** between images 240 and 295.

As demonstrated in Ref. [10], the variation of the aspect ratio of a damage site during growth sequence confirmed that it is not possible to monitor damage depth using only the fraction of damage diameter. The depth estimator based on the damage diameter fraction provided a rough depth estimation, but did not not allow uncorrelated changes in diameter and depth to be described (as for site 1).

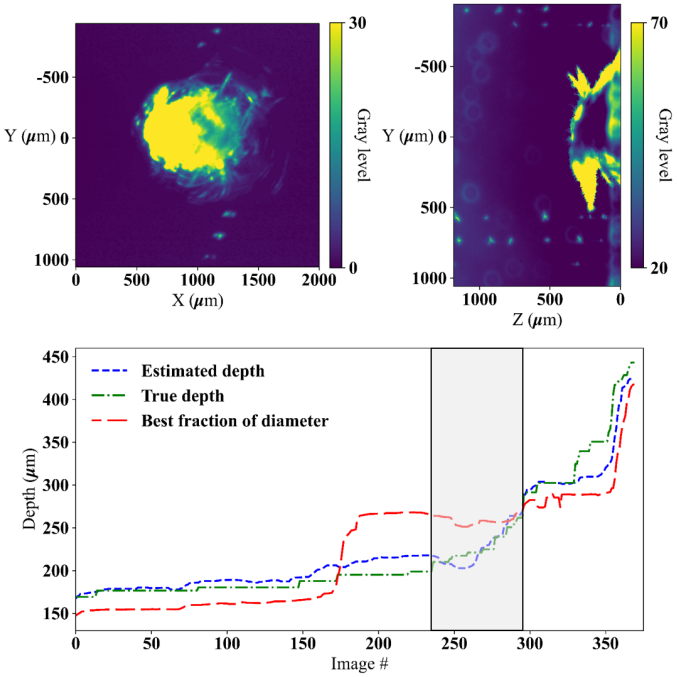

Fig. 3. Damage depth as a function of laser shot number for damage site 1; true depth in green, best fraction of diameter in red and estimated depth using the proposed estimator of Equation (5). A Veinhard plateau is observed between images 240 and 295 corresponding to damage growth in the bulk and not on the surface. The best fit is obtained with a spherical dome modeling (Equation (5)) despite the uncommon growth behavior. Bulk and surface images were acquired on site 1 after shot # 413/413 (i.e. the last laser shot of the sequence of **Visualization 1**).

The depth estimator based on the assumption that the scattered light intensity of a damage site is proportional to its volume (Equation (4)) yielded good results throughout the shooting sequences for all 4 damage sites. The R^2 scores were nearly identical for the 4 sites (*i.e.,* varying between 0.95 and 0.96). Such R^2 scores were slightly lower than those obtained by the best fraction of diameters for sites 2, 3 and 4 but higher for site 1. These results demonstrate the efficiency of the proposed depth estimator, even when the studied damage site follows so-called Veinhard plateau phases. The estimated depths using the proposed method were similar to that measured by imaging the edge of the sample. The proposed method may avoid bulk observations of a damage site by the edge, which is time consuming because of the need to polish one edge. It is worth noting that the proposed method allows for measurements of the depth for all damage sites, not just sites on the edge of the sample, as opposed to edge observation.

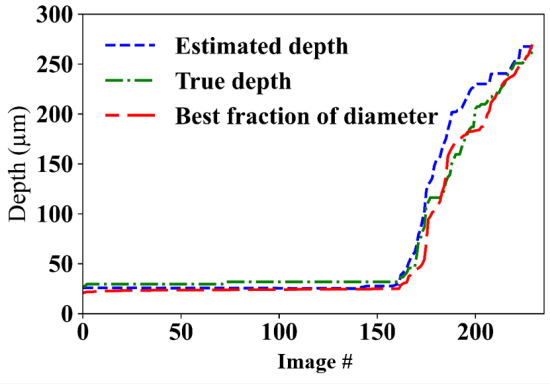

Fig. 4. Damage depth as a function of laser shot number for damage site 4; true depth in green, best fraction of diameter in red and estimated depth using the proposed estimator of Equation (5). In the present case, both estimators yielded similar results

4. Conclusion

The laser damage growth experiments described in the present work showed that the conventional proportionality between damage diameter and depth was not accurate for every growing site. Such relationship was modified using the hypothesis that the scattered light of a damage site was proportional to its volume. From this hypothesis, the damage depth was written as a function of damage diameter *and* intensity of scattered light.

Gray levels in surface images were an efficient indicator of damage growth on the surface and in the bulk even in cases when damage areas appeared constant through counting the number of lit pixels. By only using the damage size on surface images as a damage growth indicator, laser damage sequence experimenters may take the risk of considering a damage site as still, even though it grows predominantly in its bulk (*i.e.,* Veinhard plateau phases). The damage growth probabilities may therefore be underestimated. The analysis of gray levels in surface images allowed this pitfall to be avoided. It was demonstrated that increasing damage depth with constant diameter was observable only with surface images by taking into account gray level variations. The damage depth was quantitatively estimated for four damage sites using only the sum of pixel intensities and damage diameter.

In this paper, damage depth was estimated from TIS and damage diameter for a specific observation system but the method could be extended to different spatial resolutions, dynamic range or even other lighting systems. These parameters of the imaging and illumination system may have a significant impact on the measurement performance. These points may be the subject of further investigation knowing that damage observation systems differ from one laser damage testing setup to another. The description of the shape of a laser damage site by a spherical dome could also be refined to improve the accuracy of the proposed method for estimating damage depth. It would also be interesting to take into account cracks in the damage site, using for example fractal dimensions [16].

The results presented in this article pave the way for fast and accurate damage depth estimation with no need for complex instruments or time-consuming preparation of the sample. This easy access to the depth of damage sites may, among other things, bring an additional dimension to laser damage studies. The proof of concept focused on laser damage testing setup, but the application field could be extended to other domains where accurate and fast monitoring of transparent media is necessary (*e.g.,* glass and windshield industries).

Acknowledgments. The authors would like to thank Martin Cormier, Nadja Roquin and Jean-François Gleyze for the technical preparation of the laser setup. The authors also thank Nicolas Bonod and Jean-Yves

Natoli for insightful discussions.

Disclosures. The authors declare no conflicts of interest.

Data availability. Data underlying the results presented in this paper are not publicly available at this time but may be obtained from the authors upon reasonable request.

References

1. L. Lamaignère, G. Dupuy, A. Bourgeade, A. Benoist, A. Roques, and R. Courchinoux, "Damage growth in fused silica optics at 351 nm: refined modeling of large-beam experiments," Appl. Phys. B: Lasers Opt. **114**, 517–526 (2014).
2. K. Manes, M. Spaeth, J. Adams, and M. Bowers, "Damage mechanisms avoided or managed for nif large optics," Fusion Sci. Technol. **69**, 146–249 (2016).
3. M. L. Spaeth, P. J. Wegner, T. I. Suratwala, M. C. Nostrand, J. D. Bude, A. D. Conder, J. A. Folta, J. E. Heebner, L. M. Kegelmeyer, B. J. MacGowan, D. C. Mason, M. J. Matthews, and P. K. Whitman, "Optics recycle loop strategy for nif operations above uv laser-induced damage threshold," Fusion Sci. Technol. **69**, 265–294 (2016).
4. C. Lacombe, L. Lamaignère, G. Hallo, M. Sozet, T. Donval, G. Razé, C. Ameil, M. Benoit, F. Gaudfrin, E. Bordenave, N. Bonod, and J. Néauport, "Full-scale optic designed for onsite study of damage growth at the laser megajoule facility," Opt. Express **31**, 4291–4305 (2023).
5. M. A. Norton, L. W. Hrubesh, Z. Wu, E. E. Donohue, M. D. Feit, M. R. Kozlowski, D. Milam, K. P. Neeb, W. A. Molander, A. M. Rubenchik, W. D. Sell, and P. J. Wegner, "Growth of laser-initiated damage in fused silica at 351 nm," in *Laser-Induced Damage in Optical Materials: 2000,* vol. 4347 G. J. Exarhos, A. H. Guenther, M. R. Kozlowski, K. L. Lewis, and M. J. Soileau, eds., International Society for Optics and Photonics (SPIE, 2001), pp. 468 – 468.
6. R. Courchinoux, G. Raze, C. Sudre, M. A. Josse, A. C. L. Boscheron, C. Lepage, E. Mazataud, E. Bordenave, L. Lamaignere, M. Loiseau, T. Donval, and H. Bercegol, "Laser-induced damage growth with small and large beams: comparison between laboratory experiments and large-scale laser data," in *Laser-Induced Damage in Optical Materials: 2003,* vol. 5273 G. J. Exarhos, A. H. Guenther, N. Kaiser, K. L. Lewis, M. J. Soileau, and C. J. Stolz, eds., International Society for Optics and Photonics (SPIE, 2004), pp. 99 – 106.
7. L. Lamaignere, S. Reyne, M. Loiseau, J.-C. Poncetta, and H. Bercegol, "Effects of wavelengths combination on initiation and growth of laser-induced surface damage in SiO2," in *Laser-Induced Damage in Optical Materials: 2007,* vol. 6720 G. J. Exarhos, A. H. Guenther, K. L. Lewis, D. Ristau, M. J. Soileau, and C. J. Stolz, eds., International Society for Optics and Photonics (SPIE, 2007), pp. 150 – 158.
8. R. A. Negres, M. A. Norton, D. A. Cross, and C. W. Carr, "Growth behavior of laser-induced damage on fused silica optics under uv, ns laser irradiation," Opt. Express **18**, 19966–19976 (2010).
9. M. A. Norton, E. E. Donohue, W. G. Hollingsworth, M. D. Feit, A. M. Rubenchik, and R. P. Hackel, "Growth of laser initiated damage in fused silica at 1053 nm," in *Laser-Induced Damage in Optical Materials: 2004,* vol. 5647 G. J. Exarhos, A. H. Guenther, N. Kaiser, K. L. Lewis, M. J. Soileau, and C. J. Stolz, eds., International Society for Optics and Photonics (SPIE, 2005), pp. 197 – 205.
10. M. A. Norton, J. J. Adams, C. W. Carr, E. E. Donohue, M. D. Feit, R. P. Hackel, W. G. Hollingsworth, J. A. Jarboe, M. J. Matthews, A. M. Rubenchik, and M. L. Spaeth, "Growth of laser damage in fused silica: Diameter to depth ratio," Proc. SPIE - The Int. Soc. for Opt. Eng. **6720** (2008).
11. J. Han, Q. Zhang, R. Niu, G. Feng, Y. Li, L. Yang, and C. He, "Effects of laser plasma on damage in optical glass induced by pulsed lasers," Opt. Eng. **51**, 121809 (2012).
12. T. Doualle, L. Gallais, S. Monneret, S. Bouillet, A. Bourgeade, C. Ameil, L. Lamaignère, and P. Cormont, "CO2 laser microprocessing for laser damage growth mitigation of fused silica optics," Opt. Eng. **56**, 1 – 9 (2016).
13. S. Palmier, L. Gallais, M. Commandré, P. Cormont, R. Courchinoux, L. Lamaignère, J.-L. Rullier, and P. Legros, "Optimization of a laser mitigation process in damaged fused silica," Appl. Surf. Sci. **255**, 5532–5536 (2009).
14. J. H. Campbell, P. A. Hurst, D. D. Heggins, W. A. Steele, and S. E. Bumpas, "Laser-induced damage and fracture in fused silica vacuum windows," in *Laser-Induced Damage in Optical Materials: 1996,* vol. 2966 H. E. Bennett, A. H. Guenther, M. R. Kozlowski, B. E. Newnam, and M. J. Soileau, eds., International Society for Optics and Photonics (SPIE, 1997), pp. 106 – 125.
15. C. A. Klein, "High-energy laser windows: case of fused silica," Opt. Eng. **49**, 091006 (2010).
16. M. Veinhard, O. Bonville, R. Courchinoux, R. Parreault, J.-Y. Natoli, and L. Lamaignère, "Parametric study of laser-induced damage growth in fused silica optics with large beams at 351nm. part 2: fractal analysis," Appl. Opt. **59**, 9652–9659 (2020).
17. R. A. Negres, D. A. Cross, Z. M. Liao, M. J. Matthews, and C. W. Carr, "Growth model for laser-induced damage on the exit surface of fused silica under uv, ns laser irradiation," Opt. Express **22**, 3824–3844 (2014).
18. R. Catrin, J. Neauport, P. Legros, D. Taroux, T. Corbineau, P. Cormont, and C. Maunier, "Using sted and elsm confocal microscopy for a better knowledge of fused silica polished glass interface," Opt. Express **21**, 29769–29779 (2013).
19. D. André, M. Jebahi, I. Iordanoff, J.-l. Charles, and J. Néauport, "Using the discrete element method to simulate brittle fracture in the indentation of a silica glass with a blunt indenter," Comput. Methods Appl. Mech. Eng. **265**, 136–147 (2013).

20. A. Conder, J. Chang, L. Kegelmeyer, M. Spaeth, and P. Whitman, "Final optics damage inspection (FODI) for the National Ignition Facility," in *Optics and Photonics for Information Processing IV,* vol. 7797 A. A. S. Awwal, K. M. Iftekharuddin, and S. C. Burkhart, eds., International Society for Optics and Photonics (SPIE, 2010), pp. 167 – 178.
21. M. Veinhard, "Endommagement surfacique de la silice avec des faisceaux laser de type lmj," Ph.D. thesis (2019). Thèse de doctorat dirigée par Natoli, Jean-Yves et Lamaignère, Laurent Physique et sciences de la matière. Optique, photonique et traitement d'image Aix-Marseille 2019.
22. G. Hallo, C. Lacombe, R. Parreault, N. Roquin, T. Donval, L. Lamaignère, J. Néauport, and F. Hild, "Sub-pixel detection of laser-induced damage and its growth on fused silica optics using registration residuals," Opt. Express **29**, 35820–35836 (2021).
23. L. Lamaignère, M. Veinhard, F. Tournemenne, C. Bouyer, R. Parreault, R. Courchinoux, J. Y. Natoli, C. Rouyer, and S. Bouillet, "A powerful tool for comparing different test procedures to measure the probability and density of laser induced damage on optical materials," Rev. Sci. Instruments **90**, 125102 (2019).
24. M. Veinhard, O. Bonville, R. Courchinoux, R. Parreault, J.-Y. Natoli, and L. Lamaignère, "MELBA: a fully customizable laser for damage experiments," in *Laser-Induced Damage in Optical Materials 2017,* vol. 10447 G. J. Exarhos, V. E. Gruzdev, J. A. Menapace, D. Ristau, and M. Soileau, eds., International Society for Optics and Photonics (SPIE, 2017), pp. 151 – 157.
25. M. Veinhard, O. Bonville, S. Bouillet, R. Courchinoux, R. Parreault, J.-Y. Natoli, and L. Lamaignère, "Parametric study of laser-induced damage growth in fused silica optics with large beams at 351nm. Part 1: stochastic approach," Appl. Opt. **59**, 9643–9651 (2020).
26. A. Ollé, J. Luce, N. Roquin, C. Rouyer, M. Sozet, L. Gallais, and L. Lamaignère, "Implications of laser beam metrology on laser damage temporal scaling law for dielectric materials in the picosecond regime," Rev. Sci. Instruments **90**, 073001 (2019).
27. K. Gaudfrin, R. Diaz, G. Beaugrand, S. Bucourt, and R. Kling, "Adaptive optics for intra-volume engraving of glass with ultra-short laser pulses," Int. Congr. on Appl. Lasers & Electro-Optics **2017**, M405 (2017).
28. G. Hallo, C. Lacombe, J. Néauport, and F. Hild, "Detection and Tracking of Laser Damage Sites on Fused Silica Components by Digital Image Correlation," Opt. Lasers Eng. **146**, 106674 (2021).
29. F. Hild and S. Roux, "Digital image correlation," in *Optical Methods for Solid Mechanics. A Full-Field Approach,* P. Rastogi and E. Hack, eds. (Wiley-VCH, Weinheim (Germany), 2012), pp. 183–228.
30. V. Sciuti, R. Canto, J. Neggers, and F. Hild, "On the benefits of correcting brightness and contrast in global digital image correlation: Monitoring cracks during curing and drying of a refractory castable," Opt. Lasers Eng. **136**, 106316 (2021).
31. Y. Sato, S. Nakajima, N. Shiraga, H. Atsumi, S. Yoshida, T. Koller, G. Gerig, and R. Kikinis, "Three-dimensional multi-scale line filter for segmentation and visualization of curvilinear structures in medical images," Med. Image Analysis **2**, 143–168 (1998).
32. K. Pearson, "Notes on regression and inheritance in the case of two parents," Proc. Royal Soc. Lond. **58**, 240–242 (1895).
33. N. Otsu, "A threshold selection method from gray-level histograms," IEEE Transactions on Syst. Man, Cybern. **9**, 62–66 (1979).
34. G. Hallo, C. Lacombe, M. Fouchier, M. Zerrad, J. Néauport, and F. Hild, "Optical model-based calibration of gray levels for laser damage size assessment," To be published Opt. Lett. (2022).
35. T. Yeo, S. Ong, Jayasooriah, and R. Sinniah, "Autofocusing for tissue microscopy," Image Vis. Comput. **11**, 629–639 (1993).

Appendix: Registration procedure

The metric used to evaluate the efficiency of image corrections was the Root Mean Square (RMS) residual [29]. The RMS residual is the normalized quadratic norm of the difference between the reference and the corrected image over zones of interest, expressed as a percentage of the dynamic range of the reference image. For each sequence, the first image was used as the reference.

The first step of image corrections was to define the fiducial zones that were used as references. Two different fiducial masks were created, both shown for site 1 in Figure 5. The first one, type A, was composed of large rectangles containing the bulk fiducials. The second one, type B, was defined through Otsu thresholding to tightly segment bulk fiducials [33]. Type A was used for spatial registration in the same way as in Ref. [34]. Type B was dedicated to brightness and contrast corrections [28]. It was assumed that lighting variations affected the fiducial pixels (type B) the same way as the pixels of damaged sites while it may not be the same for the pixels corresponding to bulk silica (background). Some fiducials were not included in these masks as they ended up being absorbed by the main damage site during the growth sequence. Such fiducials were not suitable as reference markers. For consistency and comparison purposes, all

displayed RMS residuals were calculated on type B fiducial zones, even if the correction itself was based on type A zones.

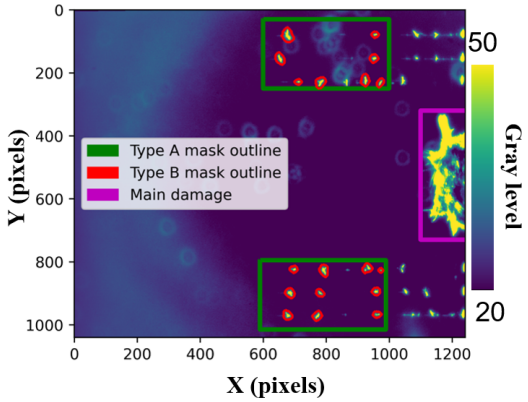

Fig. 5. Outline of type A (resp. B) fiducial masks in green rectangles (resp. red contours) and main growing damage site in the magenta rectangle. Example from volume image # 250/412 of site 2.

First, the volume images of one damage site were used to exemplify the proposed corrections, before moving to less complex surface images. Camera motions between images may arise due to vibrations, or hysteresis in the motorized systems of the cameras. Digital Image Correction was used to estimate the displacement field $\boldsymbol{u}$ between reference image I_0 and subsequent image I_n. By decomposing the displacement field on a selected basis consisting of 4 fields (*i.e.,* rigid body translations and rotation, as well as scale changes) [28], the cost function

$$\Phi_{\mathrm{A}}^2 = \sum_{\mu_{\mathrm{A}}} \left[(I_n(\boldsymbol{x} + \boldsymbol{u}(\boldsymbol{x})) - I_0(\boldsymbol{x}) \right]^2 \tag{6}$$

was minimized over the type A fiducial mask μ_{A} (Figure 5) with respect to the unknown amplitudes associated with the kinematic basis with a Gauss-Newton method [29].

As shown in Figure 6(a), the image registration procedure decreased the RMS residual on fiducial zones, making it less than 3% of dynamic range. However, several jumps in the residuals remained, corresponding to discontinuities in the estimated kinematic parameters (Figure 6(b)). It is worth noting that such discontinuities occurred only when the system had to be reset, moving the cameras back into place and turning off the LED bar. They were also associated with significant time gaps, during which spurious lighting variations may have arisen, explaining why the residual variations were still visible after correction for camera motions. Changes in the way the sample was illuminated led to differences in gray levels of the images. To correct such variations, brightness and contrast fields b and c were introduced in the cost function [30]. In order to minimize the cost function $\Phi_{\mathrm{B}}^2 = \sum_{\mu_{\mathrm{B}}} \left[(1 + c(\mathbf{x})) I_n(\boldsymbol{x} + \boldsymbol{u}(\boldsymbol{x})) + b(\mathbf{x}) - I_0(\mathbf{x}) \right]^2$, b and c were decomposed on a polynomial basis of low degree (2 in the present case). The amplitudes of brightness and contrast fields were estimated by solving a linear system [28]. Here, the summation was performed on the type B fiducial mask μ_{B} (Figure 5), as the camera acquired images of the light scattered by damage sites. Therefore, it was assumed that fiducials provided a similar response to illumination changes as the main damage sites, while that of bulk silica was different. Such differences required to use tightly segmented fiducials for an accurate estimation of the brightness and contrast fields on the damage site.

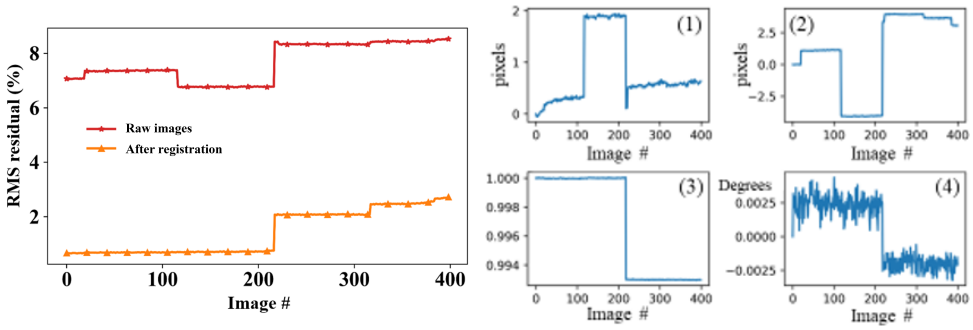

(a) (b)

Fig. 6. (a) Normalized RMS residual on type B zones before (red) and after displacement correction (orange). Kinematic parameters estimated during the displacement correction process via Digital Image Correlation: (b-1) vertical translation in pixels, (b-2) horizontal translation in pixels, (b-3) scaling and (b-4) rotation in degrees.

The last correction was related to camera focus and consequently to image sharpness. The Tenengrad function on the segmented fiducials was used to estimate image sharpness [35]. Then images were convolved by a Gaussian kernel whose standard deviation was adjusted to equalize sharpness levels throughout the image sequence. Another effect of such correction was an overall decrease in RMS residual values since the convolution smoothed out acquisition noise. After displacement, brightness, contrast and sharpness corrections, variations in the RMS residual levels remained, as observed in Figure 7, but their amplitude decreased more than five-fold thanks to the efficient image processing pipeline.

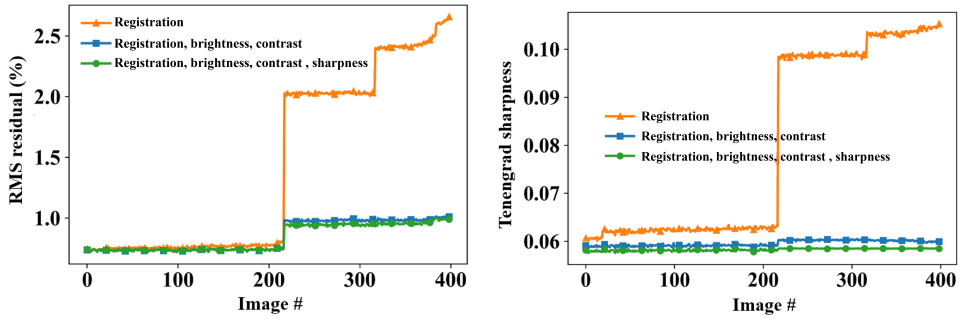

(a) (b)

Fig. 7. (a) Normalized RMS residual on type B zones after displacement (orange), brightness and contrast (blue) and sharpness (green) correction for volume images. (b) Tenengrad sharpness on type B zones after displacement (orange), brightness and contrast (blue) and sharpness (green) corrections.

The surface images required less complex corrections than the set of volume images. As shown in Figure 8, after displacement and gray level corrections, no significant residual variations remained. Therefore, no further corrections were applied to surface images.

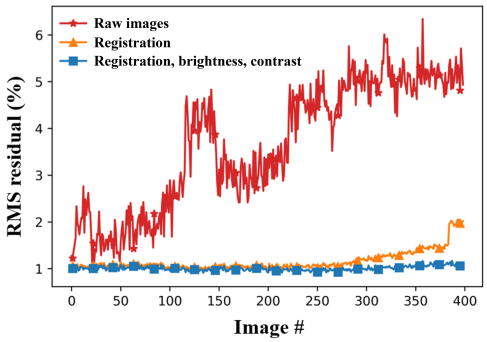

Fig. 8. Normalized RMS residual on type B zones for surface images before (red), after displacement (orange) and after brightness and contrast correction (blue) for surface images.